Irradiation-induced reactions at the CeO₂/SiO₂/Si interface

View Online   Export Citation   CrossMark

Pitambar Sapkota,[1,2] Ani Aprahamian,[1] Kwong Yu Chan,[3] Bryce Frentz,[4] Kevin T. Macon,[4]
Sylwia Ptasinska,[1,2] Daniel Robertson,[4] and Khachatur Manukyan[4,a]

AFFILIATIONS

[1] Department of Physics, University of Notre Dame, Notre Dame, Indiana 46556, USA
[2] Notre Dame Radiation Laboratory, University of Notre Dame, Notre Dame, Indiana 46556, USA
[3] Department of Chemistry, University of Hong Kong, Pokfulam, Hong Kong
[4] Nuclear Science Laboratory, University of Notre Dame, Notre Dame, Indiana 46556, USA

Note: This article is part of the JCP Special Topic on Oxide Chemistry and Catalysis.
[a] Author to whom correspondence should be addressed: kmanukya@nd.edu

ABSTRACT

The influence of high-energy (1.6 MeV) Ar^{2+} irradiation on the interfacial interaction between cerium oxide thin films (~15 nm) with a SiO_2/Si substrate is investigated using transmission electron microscopy, ultrahigh vacuum x-ray photoelectron spectroscopy (XPS), and a carbon monoxide (CO) oxidation catalytic reaction using ambient pressure XPS. The combination of these methods allows probing the dynamics of vacancy generation and its relation to chemical interactions at the $CeO_2/SiO_2/Si$ interface. The results suggest that irradiation causes amorphization of some portion of CeO_2 at the $CeO_2/SiO_2/Si$ interface and creates oxygen vacancies due to the formation of Ce_2O_3 at room temperature. The subsequent ultra-high-vacuum annealing of irradiated films increases the concentration of Ce_2O_3 with the simultaneous growth of the SiO_2 layer. Interactions with CO molecules result in an additional reduction of cerium and promote the transition of Ce_2O_3 to a silicate compound. Thermal annealing of thin films exposed to oxygen or carbon monoxide shows that the silicate phase is highly stable even at 450 °C.

Published under license by AIP Publishing. https://doi.org/10.1063/1.5142619

I. INTRODUCTION

Cerium oxide (CeO_2) has a cubic fluoride-type crystal structure. It has been widely considered for applications in catalysis[1–9] and solid oxide fuel cell developments.[10–13] In microelectronics, CeO_2 is an attractive gate layer with a high dielectric constant, dielectric strength, and a moderate bandgap.[14–18] CeO_2 is also a non-radioactive surrogate for investigating potential nuclear fuels[19–23] because it has the same crystal structure as both uranium dioxide (UO_2) and plutonium dioxide (PuO_2), exhibiting a similar irradiation defect evolution mechanism.[22]

CeO_2 is capable of releasing and absorbing oxygen due to the creation and annihilation of oxygen vacancies,[24–28] with Ce^{4+} being the preferential oxidation state. Upon heating, CeO_2 releases oxygen and anion-deficiencies are formed, which, in turn, increases the diffusion rate of anions in the lattice and leads to enhanced ionic conductivity. Both nanoscale CeO_2 particles and thin films exhibited higher Ce^{3+} concentrations than microscale CeO_2 simply from the increased surface area.[28–30]

Many model studies have been reported to investigate the generation and annihilation of oxygen vacancies using thin-film configurations.[30–34] High-energy ion irradiation was proposed to tailor the oxygen vacancy formation in cerium oxide thin films.[19,21,22,31,35,36] For example, Zhang *et al.*[22] and Edmondson *et al.*[36] reported the 3 MeV Au^+ irradiation (up to an ion fluence of 6.4×10^{15} ions/cm²) of 300 nm thick nanostructured CeO_2 samples deposited on an oxidized silicon substrate at temperatures between 25 °C and 150 °C. High-resolution electron microscopy imaging suggested that the CeO_2 layer is irradiation tolerant, even though the individual grains undergo a temperature-dependent defect-stimulated growth.[36] Naganuma and Traversa used energetic Ar ion beam irradiation to tailor the Ce^{3+}/Ce^{4+} ratio in a thin (5–15 nm) CeO_2 layer deposited on a polymeric substrate.[31] The results of x-ray photoelectron spectroscopy (XPS) investigations suggest that the

irradiated films contain nearly 80% concentration of Ce^{3+} due to the formation of oxygen vacancies. Maslakov and co-authors[35] irradiated CeO_2 films (~250 nm thickness) deposited on Si substrates and bulk CeO_2 samples with Xe ions at 92 MeV (up to a fluence of 5×10^{15} ions/cm^2). The irradiation increased the Ce^{3+} concentration in the thin films more than in the bulk samples. Edmondson and co-authors[21] reported on the formation of an intermediate layer between CeO_2 films and the Si substrate in 3 MeV Au^+ irradiated samples. Electron microscopic investigation suggested that this layer consists of Ce, Si, and O due to the interfacial mixing between the CeO_2 film and the Si substrate (or SiO_2 surface layer). Taken together, these works suggest that the role of ion irradiation in tailoring the structure and generating oxygen vacancies of CeO_2 is not fully understood. There is no complete understanding of the influence of ion type, the layer thickness of CeO_2, and the possible effects of interfacial reactions between the films and substrates on the vacancy generation mechanisms.

In this work, we investigate the effect of accelerated Ar^{2+} ion irradiation of thin (~15 nm) CeO_2 films deposited on the oxidized silicon substrate. We use high-resolution transmission electron microscopy (TEM), ultra-high vacuum XPS, and ambient pressure XPS (AP-XPS) to probe the dynamics of vacancy generation and its relation to chemical interactions at the $CeO_2/SiO_2/Si$ interface.

II. EXPERIMENTAL DETAILS

The spin coating of colloidal CeO_2 (99.5% trace metal basis, Sigma-Aldrich) nanoparticles dispersed in water was used to deposit CeO_2 films on oxidized silicon. Si (111) wafers with 100 mm diameter were cut into 8 mm × 8 mm pieces and successively cleaned using acetone, ethanol, and isopropanol in an ultrasonic bath, followed by drying in a high-purity argon gas flow. The silicon pieces were then subjected to 5% air–argon plasma cleaning for 5 min. Preparation then was proceeded by diluting 10 ml of colloidal CeO_2 aqueous solution with 30 ml of deionized water and then adding 1 ml of acetic acid (Sigma-Aldrich, 99.95%) to the colloid. In each deposition, 50 μl of colloidal solution was pipetted to cleaned silicon pieces. The samples were then spin-coated at 2000 rpm for 30 s. After deposition, the samples were heated to 250 °C for 15 min to remove the acetic acid stabilizer.

Ion irradiation of the thin films was performed by the Ar^{2+} beam (1.6 MeV energy) up to a fluence of 1×10^{16} ions/cm^2 using the 5U single-ended accelerator at the University of Notre Dame Nuclear Science Laboratory. Irradiation of the films was done at a normal incidence over a uniformly scanned irradiation diameter of 10 mm on the samples. The ion flux was kept at ~10^{11} ion/cm^2 s to minimize the beam heating effects. The Stopping and Range of Ions in Matter (SRIM)[37] calculations provided the projected ion range to be ~800 nm, showing that approximately 99.9% of the ions pass through the CeO_2 layer and only 0.01% were trapped inside the film.

TEM and XPS techniques were used to characterize the post-irradiated samples. Cross-sectional slices from irradiated materials were taken for TEM analysis using a Helios NanoLab 600 system as previously described.[38–40] A protective platinum layer (10 μm × 7.5 μm × 2 μm) was deposited on the film surface before taking cross-sectional slices. Colloidal CeO_2 was diluted with

deionized water and drop-casted on a Cu 300 mesh TEM grid. The structure evolution of slices and colloidal CeO_2 was conducted with a Titan-300 (FEI). An AP-XPS instrument manufactured by SPECS Surface Nano Analysis GmbH, Germany, was used for conducting room temperature (RT), ultra-high-vacuum annealing (up to 500 °C) and in situ ambient pressure measurements of irradiated films during CO oxidation reaction. The description of the AP-XPS instrument was described in detail,[41] and it was also used previously to investigate H_2O and O_2 interactions with other oxide nanomaterials.[42] An Al Kα x-ray beam of the photon energy of 1486.6 eV was generated from an aluminum anode in a microfocus x-ray source equipped with a quartz crystal, which monochromatizes the x-ray beam. The beam passed through a silicon nitride window, which maintains the pressure difference between a reaction cell (~3 mbar) and an analysis chamber (~1^{-10} mbar) while allowing the x ray to reach the sample without losing the beam intensity during ambient pressure measurements. All the ejected photoelectrons passed through a skimmer with an orifice of diameter 300 μm before entering differential pumping stages, followed by a hemispherical analyzer, where the kinetic energy of the photoelectrons was analyzed. Collected photoelectrons were analyzed in the fixed analyzer transmission mode and finally counted with a 1-D delay line detector consisting of nine micro-channels. The high-resolution spectra were collected at 20 eV pass energy and calibrated by adjusting the binding energy position of the main Ce $3d_{5/2}$ peak (peak v) at 882.7 eV, which corresponds to the Ce^{4+} oxidation state.[5] In AP-XPS experiments, 1 mbar of O_2 and 2 mbar of CO were introduced into the reaction cell with the help of leak valves that could precisely control the pressure of the introduced gases.

Gas-lines were flushed with these reactant gases and argon before introducing them into the cell to ensure that they were free of contaminants. For XPS measurements, thin film samples were clamped to the molybdenum sample holder plate, while powder samples were hand-pressed over stainless steel foil, which was then clamped to the plate. Heating of the film was achieved with thermo-ionically emitted electrons that hit the rear side of a molybdenum sample holder plate, while the temperature was measured with a K-type thermocouple attached to the front side of the plate. The temperature was controlled by tuning the emission current and accelerating voltage of the thermo-ionic electrons.

III. RESULTS

A. Morphology and microstructure of films

Figure 1(a) shows TEM images of the CeO_2 deposited on a TEM grid, demonstrating that the particle sizes of colloidal CeO_2 are below 5 nm. The electron diffraction pattern [inset in Fig. 1(a)] reveals that the nanoparticles are also highly crystalline. A scanning electron microscope (SEM) image (plane view) of the as-prepared sample shows the porous CeO_2 layer deposited on the substrate [Fig. 1(b)], with the thickness of the CeO_2 layer to be of 16 nm ± 1 nm determined by a cross-sectional SEM image [Fig. 1(c)].

Figure 2 shows the plane view SEM images of the irradiated and annealed samples. The plane view images of two irradiated samples [Figs. 2(a) and 2(b)] exhibit some porosity similar to the samples
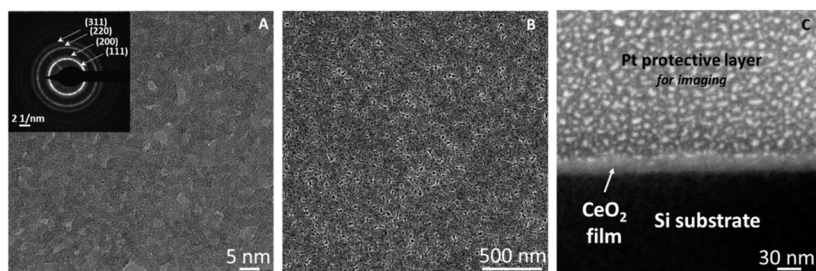
FIG. 1. Colloidal CeO$_2$ nanoparticles deposited on a TEM grid (a), a plane view (b), and a cross-sectional SEM image (c) of the CeO$_2$ film deposited on the Si substrate. The inset in (a) displays an electron diffraction pattern of CeO$_2$ nanoparticles.

before irradiation [see Fig. 1(b)]. The ultra-high-vacuum annealing at 500 °C changes the microstructure and creates some channel-like features along with some relatively large pores on the surface [Fig. 2(c)].

Figure 3 displays cross-sectional TEM images of non-irradiated (a), irradiated [(b) and (c)], and annealed (d) samples. All images show the existence of a thin amorphous interlayer between the Si substrate and the CeO$_2$ film. At least 20 TEM images were taken for each sample from different areas to obtain the thickness distribution of the SiO$_2$ interlayer. Figure 3(a) shows that the non-irradiated CeO$_2$ film has an approximately ~16 nm thickness with a random texture.

The average thickness of the SiO$_2$ interlayer between CeO$_2$ and Si is ~1.92 nm for the non-irradiated samples. The irradiated film with 1×10^{14} ion/cm^2 fluence exhibits similar morphology as the non-irradiated sample [Fig. 3(b)]. The amorphous layer is slightly thicker (2.05 nm) than the one in the non-irradiated sample. The CeO$_2$ films irradiated with 1×10^{16} ion/cm^2 fluence is less porous when compared with the other two samples [Fig. 3(c)]. This film also exhibits randomly oriented large grains closer to the surface. The average layer thickness for the SiO$_2$ interlayer is 2.47 nm. After annealing, the CeO$_2$ film becomes uneven [Fig. 3(d)]. The SiO$_2$ layer is also uneven and significantly thicker (3.29 nm) in this sample. Energy-dispersive x-ray spectroscopy (EDXS) elemental distribution of this sample confirms that this layer consists of Si and O (Fig. S1 of the supplementary material). Figure 3(d) also shows that irradiation and subsequent annealing result in significant growth of CeO$_2$ grains close to the surface. Based on these results, we can suggest that irradiation facilitates the interfacial reaction between the film and substrate, evidenced by the increase in average thickness of the interlayer.
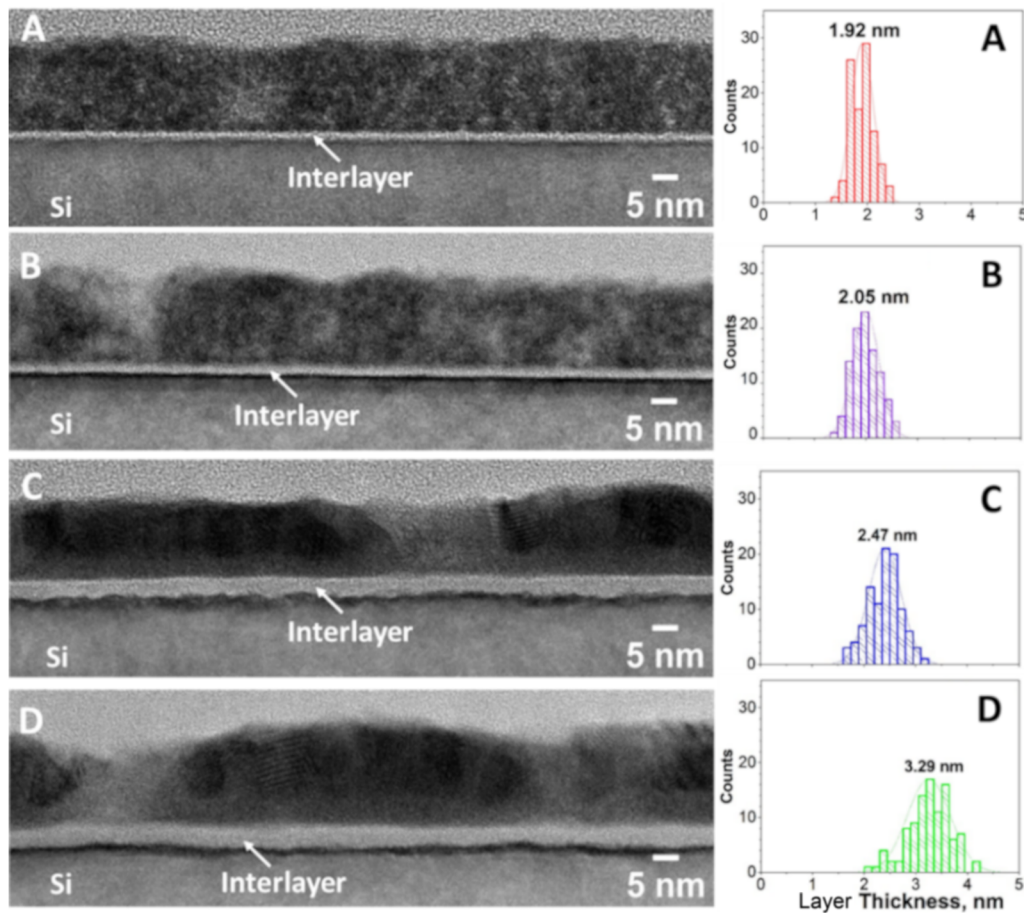
Figure 4 shows high-resolution TEM images of the same films. The image for the non-irradiated sample confirms the presence of randomly oriented CeO$_2$ crystallites [Fig. 4(a)]. The Fast Fourier Transform [FFT, inset in Fig. 4(a)] processing of the TEM image

clearly shows the rings responsible for the (111) and (220) orientations. The irradiated sample with 1×10^{14} ion/cm^2 fluence shows similar rings [Fig. 4(b)]. However, the sample irradiated with 1×10^{16} ion/cm^2 fluence shows significant differences [Fig. 4(c)]. The CeO$_2$ layer has two distinct sublayers: a crystalline surface layer (with the thickness of ~10–12 nm) and a second amorphous interlayer (3–4 nm) close to the SiO$_2$ layer. TEM and FFT images also provide evidence of some radiation-induced grain growth in the crystalline section of the CeO$_2$ film. In the irradiated then annealed (500 °C) samples, the thickness of the second amorphous layer is ~5 nm [Fig. 4(d)]. A FFT image suggests the presence of relatively large grains with an improved crystalline structure. These findings based on TEM images indicate that ion irradiation and post-irradiation annealing create a complex amorphous structure at the CeO$_2$/SiO$_2$/Si interface. On the other hand, ion irradiation induces a grain coarsening at the surface of the CeO$_2$ layer, which becomes more pronounced after post-irradiation ultra-high-vacuum annealing.

Figure 5 displays selected area electron diffraction (SAED) patterns and normalized radial intensity profiles extracted from the patterns for colloidal CeO$_2$ as well as irradiated and annealed CeO$_2$/Si samples. The profiles were generated from electron diffraction patterns using a standard method described elsewhere.[43] The SAED pattern and the profile for colloidal CeO$_2$ (profile a) indicate a typical polycrystalline structure. The intensity profile for colloidal CeO$_2$ also matches well with the simulated powder diffraction pattern of CeO$_2$ (PDF No. 65-2975). This result indicates that the CeO$_2$ nanoparticles are in a single-phase with a cubic fluoride-type crystal structure. The intensity profiles for irradiated and annealed samples (profiles b–d) exhibit broad lines of a Pt protective layer (deposited for TEM sample preparation purposes) along with some diffraction lines for CeO$_2$. It should be noted that the diffraction measurements were performed in a way to avoid taking the signal from the silicon substrate. These profiles show that increasing the radiation dose reduces the intensities of CeO$_2$ peaks. The profiles for the
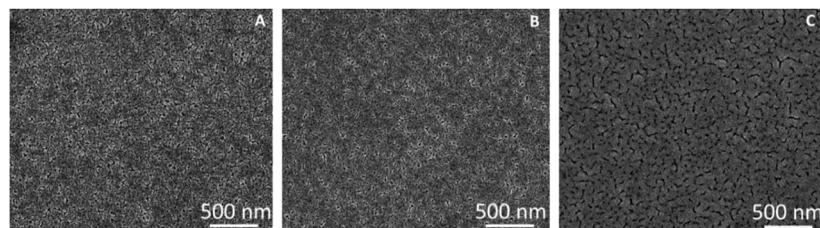
FIG. 2. Plane view SEM images of irradiated and annealed CeO$_2$/Si samples: (a) irradiated with 1×10^{14} ion/cm^2 and (b) 1×10^{16} ion/cm^2 fluences as well as the annealed sample irradiated with 1×10^{16} ion/cm^2 fluence (c).

FIG. 3. Cross-sectional high-resolution TEM images of CeO$_2$/Si films: non-irradiated (a), irradiated with 1×10^{14} ion/cm^2 (b) and 1×10^{16} ion/cm^2 (c) ion fluences, as well as annealed (d) after irradiation (1×10^{16} ion/cm^2), and thickness distributions of the interlayer measured from TEM images.

irradiated and annealed sample show that the intensity of (111) and (311) peaks increased slightly. These results confirm that the irradiation causes amorphization of some portion of CeO$_2$ while subsequent heating increases either the crystallinity or size for the remaining CeO$_2$ grains.

B. Chemical states of films

Figure 6 shows the fitted XPS Ce3d and O1s spectra of non-irradiated, irradiated, and annealed thin films at room temperature under ultra-high vacuum conditions. Multiple scans were collected for each core level, and the final spectrum was obtained by averaging the intensities from all those scans. The Ce3d spectra were fitted after subtracting the U2 Tougaard[44,45] background with five doublets labeled v and u corresponding to the spin–orbit splitting of the 3d$_{5/2}$ and 3d$_{3/2}$ states, respectively, while the O1s spectra were fitted with four peaks after subtracting the Shirley background (see the supplementary material for more details). Each of the fitted peaks had a Gaussian/Lorentzian shape with a mixing ratio of 7:3. The peaks were assigned based on previous works,[5,46–48] and their positions,

areas, and full-width half-maxima are listed in Tables S1 and S2 of the supplementary material. The doublet pairs u$_o$-v$_o$ and u$'$-v$'$ are assigned to the Ce^{3+} state, while other pairs u-v, u$''$-v$''$, and u$'''$-v$'''$ are assigned to Ce^{4+}. The Ce3d spectra for all the CeO$_2$ films show the presence of Ce in both oxidation states, i.e., +3 and +4. In Fig. 6, the Ce3d spectra [spectra (b) and (c)] clearly show that ion irradiation increases the relative contribution (47.8% and 59.9%) of Ce^{3+} in the films (low dose and high dose irradiated, respectively) compared to the non-irradiated samples [spectrum (a)], which shows only 16.6% of Ce^{3+} at room temperature. The irradiated and annealed film [spectrum (d)] exhibits even higher concentrations (60.6%) of Ce^{3+} than the one at room temperature.

The peaks A and D in the O1s spectra are assigned to Ce–O (529.7 eV $\pm$ 0.3 eV, lattice oxygen) and to Si–O (532.8 eV $\pm$ 0.3 eV) bonds in CeO$_2$ and SiO$_2$, respectively.[46] The peak B (531.0 eV $\pm$ 0.3 eV) is attributed to oxygen vacancies, which are produced when Ce$_2$O$_3$ is formed, while the peak C (532.1 eV $\pm$ 0.3 eV) is assigned to cerium silicate. For the irradiated films, insignificant changes are observed for the lattice oxygen peak in the O1s spectra [spectra (f)–(h) in Fig. 6] in comparison to changes in the peaks
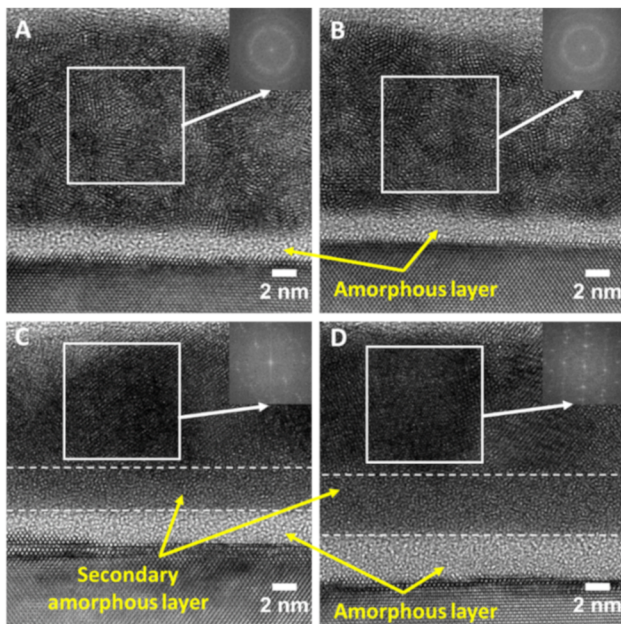
FIG. 4. High-resolution TEM images and FFT patterns of selected areas of the CeO_2 layer for the initial CeO_2/Si (a), irradiated with 1×10^{14} ion/cm^2 (b) and 1×10^{16} ion/cm^2 (c) fluences, as well as annealed (d) after irradiation (1×10^{16} ion/cm^2).

corresponding to Ce^{4+} in Ce3d. This is because of the inelastic mean free path of photoelectrons from the O1s core level ($\sim$15 Å) is larger than that from the Ce3d core level ($\sim$11 Å). Thus, the signal from the O1s photoelectrons is collected from deeper layers compared to the signal from more surface-confined Ce3d states. The results from the XPS analysis suggest that irradiation and annealing of CeO_2 thin films deposited on Si induce chemical alterations, which are more pronounced at the surface.
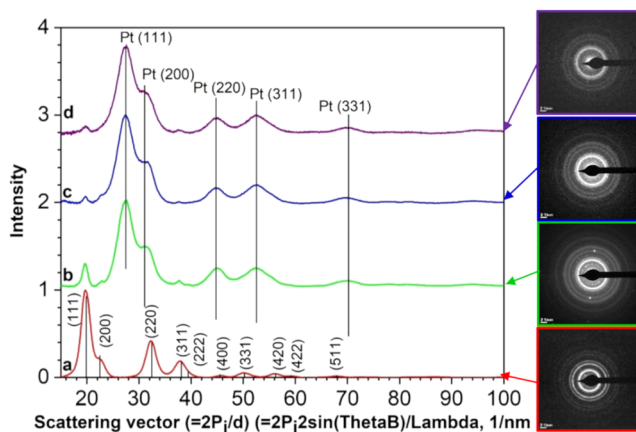
FIG. 5. Diffraction profiles calculated from selected area electron diffraction patterns (insets) for colloidal CeO_2 (a), the samples irradiated with 1×10^{14} ion/cm^2 (b) and 1×10^{16} ion/cm^2 (c) fluences, as well as (d) annealed after irradiation (1×10^{16} ion/cm^2).

The O1s spectrum for the non-irradiated films contains both types of oxygen vacancies, indicating the formation of Ce_2O_3 and cerium silicate in the sample. The presence of the cerium silicate species in the non-irradiated sample can be attributed to an interfacial reaction that could take place during heat treatment of samples after spin coating (see Sec. II). The relative intensity of the oxygen vacancy peak to that for cerium silicate increases for both irradiated samples [spectra (f) and (g)] compared to the non-irradiated one [spectrum (e)]. Moreover, the increase in ion fluence leads to an increase in oxygen vacancy relative to cerium silicate. The relative contribution of oxygen vacancy to cerium silicate in the O1s spectra becomes even more intense after the combined irradiation and annealing treatment [spectrum (h)], during which the cerium silicate peak gradually decreases with increasing temperature (see Fig. S2 of the supplementary material) and completely disappears at 500 °C. The O1s spectra for the vacuum annealed irradiated sample also show a contribution from the Si–O bond in SiO_2 (peak D). The appearance of this peak can be related to two factors: the increasing thickness of the SiO_2 interlayer, as evidenced by TEM images (see Figs. 3 and 4), and the local decrease in the CeO_2 layer thickness due to the formation of channel-like features in the film [Figs. 2(d) and 3(d)].

The XPS results indicate that irradiation predominantly creates oxygen vacancies due to the formation of Ce_2O_3, rather than silicates. The subsequent annealing of the irradiated films increases the oxygen vacancy even more along with the simultaneous growth of the SiO_2 layer, which can be formed by oxygen diffusion from the film to the substrate. Thus, this promotes the oxidation of silicon and the growth of the SiO_2 interlayer.

C. Chemical states of films and powders under *operando* conditions

We performed AP-XPS studies of the CO oxidation on irradiated and non-irradiated samples to evaluate the generation and annihilation of oxygen vacancies. This reaction has been shown to be an accurate probe of oxygen mobility in CeO_2 at high temperatures.[3,49,50] CO oxidation is also known to proceed via the Mars–van Krevelen mechanism on the CeO_2,[49,50] involving the removal of surface lattice oxygen by CO and consequent annihilation of vacancies by gas phase oxygen. We performed the *in situ* CO + O_2 reaction using AP-XPS to follow the dynamics of oxygen vacancy formation and to probe the chemical reactions at the CeO_2/SiO_2/Si interface.

The Ce3d spectra of the non-irradiated sample indicate a minor decrease in the contribution of the Ce^{3+} valence state at temperatures up to 400 °C, while it suddenly rises at 500 °C during CO + O_2 reaction [see, for example ,the relative intensities of u′and v′ in Fig. 7(a) and Fig. S5 of the supplementary material]. The O1s spectra also show a gradual decrease in the cerium silicate intensity at temperatures up to 400 °C, while at 500 °C, the oxygen vacancy intensity increases in conjunction with the disappearance the cerium silicate contribution [Fig. 7(c)]. This indicates that film oxidation occurs below 400 °C, whereas above this temperature, the oxygen vacancies form due to the $CeO_2 \rightarrow Ce_2O_3$ transformation.

The Ce3d spectrum [Fig. 7(b)] for the irradiated sample (1×10^{16} ion/cm^2) shows a significant difference in peak intensities in comparison with that for the non-irradiated annealed films. The Ce3d spectra for both irradiated and non-irradiated samples show
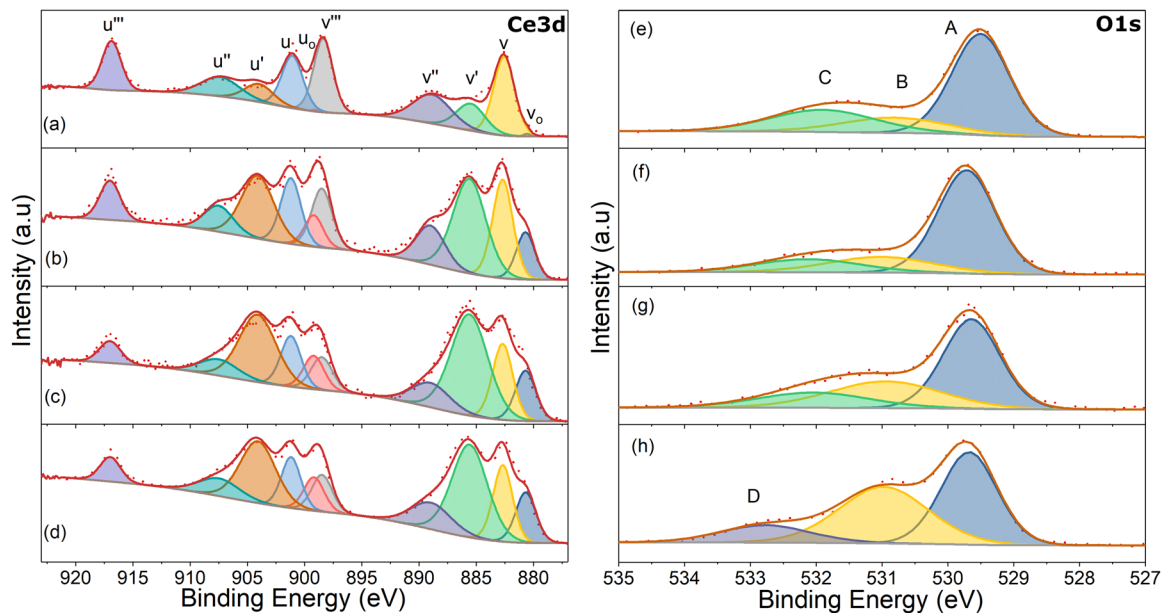
FIG. 6. Fitted room temperature, ultra-high-vacuum Ce3d and O1s spectra for CeO_2 thin films deposited on Si: non-irradiated [(a) and (e)], irradiated with 1×10^{14} ion/cm^2 [(b) and (f)] and 1×10^{16} ion/cm^2 [(c) and (g)] fluences, as well as those samples annealed in vacuum at 500 °C [(d) and (h)] after irradiation (1×10^{16} ion/cm^2).

a similar shape and trend during annealing up to 400 °C. Thus, the Ce3d spectrum [Fig. 7(b)] is evidence of a significant concentration of Ce^{3+} due to the vacancies created by ion irradiation at room temperature. Interestingly, the temperature increase from room temperature to 200 °C leads to a sudden increase in the peaks attributed to Ce^{4+}. Moreover, the increase in a peak contribution for Ce^{4+} also indicates that the film oxidizes at temperatures below 400 °C.

When the annealing temperature reaches 500 °C, the sample transforms rapidly, abruptly reducing the surface to Ce^{3+} [Fig. 7(b)
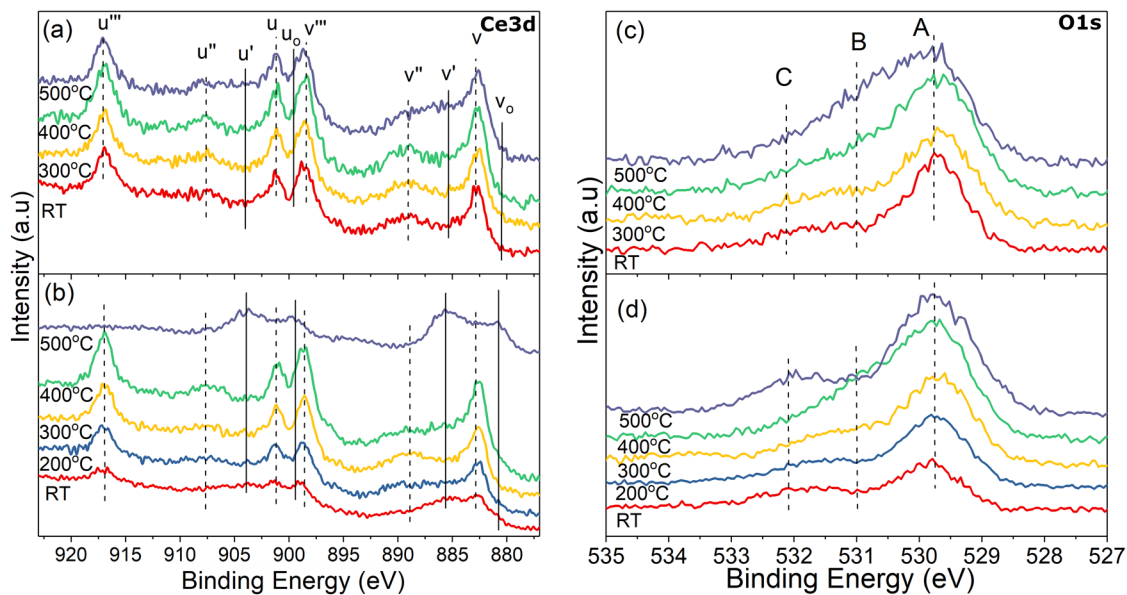
FIG. 7. AP-XPS spectra of Ce3d and O1s core level for [(a) and (c)] the non-irradiated sample and [(b) and (d)] the irradiated (1×10^{16} ion/cm^2 fluence) sample at different temperatures from room temperature (RT) until 500 °C in the presence of 1 mbar O_2 and 2 mbar CO.
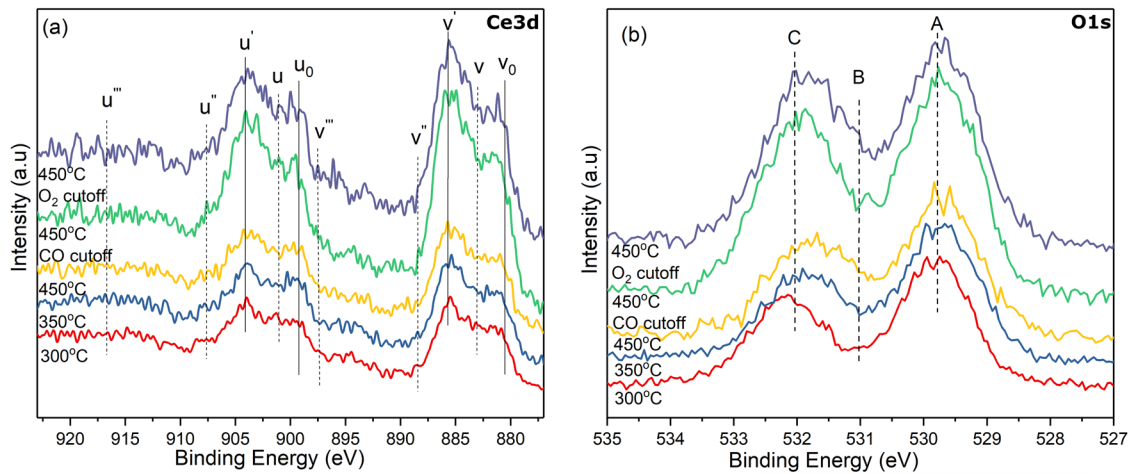
FIG. 8. Evolution of Ce3d (a) and O1s (b) spectra obtained for the irradiated (1×10^{16} ion/cm^2 fluence) samples in the second cycle of annealing in the presence of 1 mbar O_2 and 2 mbar CO or after evacuation of CO or O_2 ("cutoff" curves).

and Fig. S5 of the supplementary material]. The increasing overall contribution from lattice oxygen in the O1s spectra up to 400 °C [Fig. 7(d)] also supports the oxidation of the sample below this temperature. At the same time, the contribution from cerium silicate decreases relative to the oxygen vacancy peak. However, the cerium silicate to oxygen vacancy contribution rises at 500 °C, similar to an increase of the Ce^{3+} contribution in the Ce3d spectra. These results suggest that silicate species become dominant at 500 °C during CO + O_2 reaction in the irradiated samples.

We also conducted the second cycle of annealing from room temperature to 450 °C with CO + O_2 gas mixture flow to evaluate the stability of silicate species. Figure 8 shows both the XPS spectra from the second cycle obtained for the films after evacuation to vacuum and cooling down to room temperature from the first cycle of the experiment. The spectra for both Ce3d and O1s remained unchanged during this entire cycle of annealing in the gas mixture. Moreover, the chemical state of the film is resistant to annealing up to 450 °C in the presence of either CO or O_2 (O_2 cutoff or CO cutoff, respectively, in Fig. 8) In addition, the contribution from cerium silicate relative to oxygen vacancy in the O1s spectra is observed to increase further, suggesting some changes at the film/substrate interface.

We also investigated the CO oxidation on the irradiated and non-irradiated CeO_2 samples in the form of compressed powder (without Si substrate) to understand the role of the substrate. This also allowed confirming the origin of peaks in the O1s spectra, especially peaks B and C preliminarily assigned to oxygen vacancies and cerium silicate. The Ce3d (Fig. S3 of the supplementary material) and O1s (Fig. S4 of the supplementary material) spectra from these samples indicate that powders behave differently than thin films. The surface of these powders, either irradiated or not, is oxidized and exhibits high concentrations of Ce^{4+} oxidation state even at 500 °C (Fig. S5 of the supplementary material). Moreover, O1s spectra can be fitted with only two peaks, as shown in Fig. S4 of the supplementary material. Since there is no possibility of the formation of cerium silicate in powder samples, peak B can arise only due

to the formation of Ce_2O_3. Nevertheless, these results confirm that among the two peaks (peak B and peak C, both contributing to Ce^{3+} in O1s spectra of thin films), a lower binding energy peak (peak B) is attributed solely to oxygen vacancy due to the formation of Ce_2O_3 and a higher binding energy peak (peak C) arises from cerium silicate. The shift in the binding energy of the O1s spectrum at room temperature is attributed to local potential difference created due to the inhomogeneous distribution of nanoparticles on the surface (see the experimental section). At higher temperatures, these nanoparticles get sufficient thermal energy to diffuse on the surface, thus rearranging themselves and forming a homogeneous distribution, which removes the shift observed in the binding energy of O1s spectrum at room temperature.

IV. DISCUSSION

The interfacial reactions between the CeO_2 films and Si substrate were observed in prior studies during post-deposition heat treatment without using ion irradiation. For example, Preisler et al.[48] used the XPS technique to reveal the effect of temperature on the interfacial reaction between the CeO_2 films (3–4 nm) on a Si substrate. Ultra-high-vacuum annealing showed no chemical changes below 570 °C. The $Ce^{4+} \rightarrow Ce^{3+}$ transition was observed in the 570–620 °C interval. Yoo and co-authors[51] investigated annealing of a 10–15 nm thick polycrystalline CeO_2 layer in an oxygen atmosphere and also showed the existence of an amorphous SiO_2 layer between the CeO_2 film and the Si substrate.

Iordanova and co-authors[52] reported a magnetron sputtering deposition of CeO_2 films (100–140 nm) on a silicon substrate heated to 700 °C. Annealing of samples at 1100 °C resulted in the formation of CeO_2, Ce_2O_3, and SiO_2 polycrystalline phases. The authors also showed that CeSi and $CeSi_2$ compounds formed during annealing. Luo and coauthors[53] also reported high vacuum annealing experiments with CeO_2 films (with a thickness of ~80 nm) deposited on Si substrates. They noted that the increase in the temperature to 730 °C led to an increase in Ce^{3+} concentration. However, the

complete $Ce^{4+} \rightarrow Ce^{3+}$ transition was not observed, even following long annealing times, up to a few hours.

Pagliuca et al.[46] deposited CeO_2 films (1–3 nm) with different thicknesses on thermally oxidized silicon (500 nm SiO_2 layer thickness). They suggested that the reaction between CeO_2 and SiO_2/Si produces a silicate phase with a sub-nanometric thickness. Vorokhta and co-authors[54] suggested that the presence of native SiO_2 on the Si substrate hinders the interaction between the CeO_2 film (1–20 nm) and the Si substrate. Anandan and Bera also showed the presence of both Ce^{4+} and Ce^{3+} oxidation states in CeO_2 films (with about 25 nm thickness) deposited on Si substrates.[55,56] Based on XPS analysis, they suggested that Ce_2O_3 and SiO_x or cerium silicate type species were formed at the interface. Vacuum annealing at 400–600 °C resulted in an increase of the Ce^{3+} concentrations due to the enhanced interfacial reaction.

The CeO_2 deposited in films as previous studies were mainly prepared by using reactive evaporation of metallic Ce in low-pressure oxygen environments at high temperatures (200–500 °C). Such a process could facilitate mutual diffusion and accelerate chemical mixing at the film and substrate interface, even during deposition. In this work, we attempted to minimize the interaction between the film and substrate during the deposition process by using the spin coating of colloidal CeO_2 at room temperature, followed by a short heat treatment to remove acetic acid present in the colloidal solution. Our XPS analysis showed the presence of only a small amount of silicate compound after such a preparation. The effect of sample preparation in this work is minimized, and all interfacial interactions can, therefore, be attributed solely to ion irradiation and annealing.

Our results suggest that irradiation causes amorphization of some portion of CeO_2, at the $CeO_2/SiO_2/Si$ interface, and creates oxygen vacancies, even at room temperature. Edmondson et al.[21] also reported similar Au^+ ion irradiation-induced amorphization at the $CeO_2/SiO_2/Si$ interface and the formation of an intermediate layer between CeO_2 and Si. Their results, however, suggested that a silicate compound forms during the irradiation. Our XPS analysis indicates that Ar^{2+} irradiation predominantly creates oxygen vacancies due to the formation of Ce_2O_3 rather than the formation of a silicate compound. Irradiation in our case only leads to limited mixing between Ce_2O_3 and SiO_2, although we do observe a thin secondary amorphous layer formed at the interface (Fig. 4). The subsequent ultra-high-vacuum annealing to 500 °C of the irradiated sample increases the concentration of Ce_2O_3 (Fig. 6) with the simultaneous growth of the SiO_2 layer. We can, therefore, suggest that under our experimental conditions, oxygen diffuses and oxidizes the Si atoms. The difference in the interaction mechanisms can be attributed to the relatively higher Au^+ ion energy (3 MeV) used in the work of Edmondson and co-workers.[21] However, our work shows that a beam with lower energy promotes the formation of lattice vacancies, while only limited chemical mixing takes place. Interactions with CO molecules during the in situ ambient pressure XPS experiments caused an additional reduction of cerium and promoted the transition of Ce_2O_3 to a stable silicate compound. Therefore, more CeO_2 is reduced by the introduction of CO at ~500 °C during the first cycle of annealing under CO + O_2 reaction conditions. The removal of lattice oxygen by CO leads to the formation of Ce_2O_3 confirmed by the abrupt change in the Ce 3d spectrum [Fig. 7(b)]. Vacancy annihilations from the gas-phase oxygen,

however, do not take place due to the formation of a stable amorphous silicate compound, as evidenced by a significant increase in the peak intensity attributed to oxygen vacancy in the O1s spectra [Fig. 7(d)]. The second cycle of the CO + O_2 reaction shows that this process is irreversible and that the silicate phase is stable in all investigated temperatures (Fig. 8).

V. CONCLUSIONS

In summary, we performed a systematic study of irradiation-induced structural transformations on the interfacial interaction between CeO_2 films and SiO_2/Si substrates. The results of this work suggest that high-energy Ar^{2+} irradiation causes amorphization of some portion of CeO_2, at the $CeO_2/SiO_2/Si$ interface and creates oxygen vacancies due to the formation of Ce_2O_3 at room temperature. The ultra-high-vacuum annealing of the irradiated samples increases the concentration of Ce_2O_3 with the simultaneous oxidation of silicon and growth of the SiO_2 layer. Interaction with CO molecules during the ambient pressure XPS experiments causes an additional reduction of cerium and promotes the transition of Ce_2O_3 to a stable silicate compound.

SUPPLEMENTARY MATERIAL

See the supplementary material for additional TEM images, energy-dispersive x-ray spectroscopy (EDS) mapping, and XPS spectra.

REFERENCES

[1] J. W. D. Ng, M. García-Melchor, M. Bajdich, P. Chakthranont, C. Kirk, A. Vojvodic, and T. F. Jaramillo, Nat. Energy **1**, 16053 (2016).

[2] D. R. Mullins, Surf. Sci. Rep. **70**, 42 (2015).

[3] E. Aneggi, J. Llorca, M. Boaro, and A. Trovarelli, J. Catal. **234**, 88 (2005).

[4] A. A. Voskanyan, K. Y. Chan, and C. Y. V. Li, Chem. Mater. **28**, 2768 (2016).

[5] L. Artiglia, F. Orlando, K. Roy, R. Kopelent, O. Safonova, M. Nachtegaal, T. Huthwelker, and J. A. van Bokhoven, J. Phys. Chem. Lett. **8**, 102 (2017).

[6] J. S. Elias, N. Artrith, M. Bugnet, L. Giordano, G. A. Botton, A. M. Kolpak, and Y. Shao-Horn, ACS Catal. **6**, 1675 (2016).

[7] J. A. Rodriguez, D. C. Grinter, Z. Liu, R. M. Palomino, and S. D. Senanayake, Chem. Soc. Rev. **46**, 1824 (2017).

[8] S. Carrettin, P. Concepción, A. Corma, J. M. López Nieto, and V. F. Puntes, Angew. Chem., Int. Ed. **43**, 2538 (2004).

[9] K. An, S. Alayoglu, N. Musselwhite, S. Plamthottam, G. Melaet, A. E. Lindeman, and G. A. Somorjai, J. Am. Chem. Soc. **135**, 16689 (2013).

[10] S. P. S. Shaikh, A. Muchtar, and M. R. Somalu, Renewable Sustainable Energy Rev. **51**, 1 (2015).

[11] R. Fiala, M. Vaclavu, M. Vorokhta, I. Khalakhan, J. Lavkova, V. Potin, I. Matolinova, and V. Matolin, J. Power Sources **273**, 105 (2015).

[12] R. Fiala, M. Vaclavu, A. Rednyk, I. Khalakhan, M. Vorokhta, J. Lavkova, V. Potin, I. Matolinova, and V. Matolin, Catal. Today **240**, 236 (2015).

[13] C. Zhang, A. Michaelides, D. A. King, and S. J. Jenkins, J. Chem. Phys. **129**, 194708 (2008).

[14] Y. Nishikawa, T. Yamaguchi, M. Yoshiki, H. Satake, and N. Fukushima, Appl. Phys. Lett. **81**, 4386 (2002).

[15] Y. Nishikawa, N. Fukushima, N. Yasuda, K. Nakayama, and S. Ikegawa, Jpn. J. Appl. Phys. **41**, 2480 (2002).

[16] P. R. L. Keating, D. O. Scanlon, and G. W. Watson, J. Mater. Chem. C **1**, 1093 (2013).

[17] M. M. V. Chong, P. S. Lee, and A. I. Y. Tok, Mater. Sci. Eng.: B **210**, 57 (2016).

[18] J. Zhang, H. Wong, K. Kakushima, and H. Iwai, Thin Solid Films **600**, 30 (2016).

[19] A. T. Nelson, D. R. Rittman, J. T. White, J. T. Dunwoody, M. Kato, and K. J. McClellan, J. Am. Ceram. Soc. **97**, 3652 (2014).

[20] B. Ye, A. Oaks, M. Kirk, D. Yun, W. Y. Chen, B. Holtzman, and J. F. Stubbins, J. Nucl. Mater. **441**, 525 (2013).

[21] P. D. Edmondson, N. P. Young, C. M. Parish, S. Moll, F. Namavar, W. J. Weber, and Y. Zhang, J. Am. Ceram. Soc. **96**, 1666 (2013).

[22] Y. Zhang, P. D. Edmondson, T. Varga, S. Moll, F. Namavar, C. Lan, and W. J. Weber, Phys. Chem. Chem. Phys. **13**, 11946 (2011).

[23] K. Suzuki, M. Kato, T. Sunaoshi, H. Uno, U. Carvajal-Nunez, A. T. Nelson, and K. J. McClellan, J. Am. Ceram. Soc. **102**, 1994 (2019).

[24] X. D. Zhou and W. Huebner, Appl. Phys. Lett. **79**, 3512 (2001).

[25] H. Hojo, T. Mizoguchi, H. Ohta, S. D. Findlay, N. Shibata, T. Yamamoto, and Y. Ikuhara, Nano Lett. **10**, 4668 (2010).

[26] X. Liu, K. Zhou, L. Wang, B. Wang, and Y. Li, J. Am. Chem. Soc. **131**, 3140 (2009).

[27] C. L. Corkhill, D. J. Bailey, F. Y. Tocino, M. C. Stennett, J. A. Miller, J. L. Provis, K. P. Travis, and N. C. Hyatt, ACS Appl. Mater. Interfaces **8**, 10562 (2016).

[28] B. Choudhury and A. Choudhury, Mater. Chem. Phys. **131**, 666 (2012).

[29] F. Zhang, S. W. Chan, J. E. Spanier, E. Apak, Q. Jin, R. D. Robinson, and I. P. Herman, Appl. Phys. Lett. **80**, 127 (2002).

[30] W. Xiao, Q. Guo, and E. G. Wang, Chem. Phys. Lett. **368**, 527 (2003).

[31] T. Naganuma and E. Traversa, Nanoscale **4**, 4950 (2012).

[32] I. W. Park, J. Lin, J. J. Moore, M. Khafizov, D. Hurley, M. V. Manuel, and T. Allen, Surf. Coat. Technol. **217**, 34 (2013).

[33] V. Fernandes, P. Schio, A. J. A. de Oliveira, W. A. Ortiz, P. Fichtner, L. Amaral, I. L. Graff, J. Varalda, N. Mattoso, W. H. Schreiner, and D. H. Mosca, J. Phys.: Condens. Matter **22**, 216004 (2010).

[34] J. P. Nair, E. Wachtel, I. Lubomirsky, J. Fleig, and J. Maier, Adv. Mater. **15**, 2077 (2003).

[35] K. I. Maslakov, Y. A. Teterin, A. J. Popel, A. Y. Teterin, K. E. Ivanov, S. N. Kalmykov, V. G. Petrov, P. K. Petrov, and I. Farnan, Appl. Surf. Sci. **448**, 154 (2018).

[36] P. D. Edmondson, Y. Zhang, S. Moll, F. Namavar, and W. J. Weber, Acta Mater. **60**, 5408 (2012).

[37] J. F. Ziegler, M. D. Ziegler, and J. P. Biersack, Nucl. Instrum. Methods Phys. Res., Sect. B **268**, 1818 (2010).

[38] K. Manukyan, C. Fasano, A. Majumdar, G. F. Peaslee, M. Raddell, E. Stech, and M. Wiescher, Appl. Surf. Sci. **493**, 818 (2019).

[39] K. V. Manukyan, W. Tan, R. J. deBoer, E. J. Stech, A. Aprahamian, M. Wiescher, S. Rouvimov, K. R. Overdeep, C. E. Shuck, T. P. Weihs, and A. S. Mukasyan, ACS Appl. Mater. Interfaces **7**, 11272 (2015).

[40] K. V. Manukyan, J. M. Pauls, C. E. Shuck, S. Rouvimov, A. S. Mukasyan, K. Nazaretyan, H. Chatilyan, and S. Kharatyan, J. Phys. Chem. C **122**, 27082 (2018).

[41] X. Zhang and S. Ptasinska, J. Phys. Chem. C **118**, 4259 (2014).

[42] T. X. T. Sayle, F. Caddeo, X. Zhang, T. Sakthivel, S. Das, S. Seal, S. Ptasinska, and D. C. Sayle, Chem. Mater. **28**, 7287 (2016).

[43] J. L. Lábár, Microsc. Microanal. **14**, 287 (2008).

[44] S. Tougaard, Surf. Interface Anal. **25**, 137 (1997).

[45] C. M. Sims, R. A. Maier, A. C. Johnston-Peck, J. M. Gorham, V. A. Hackley, and B. C. Nelson, Nanotechnology **30**, 085703 (2019).

[46] F. Pagliuca, P. Luches, and S. Valeri, Surf. Sci. **607**, 164 (2013).

[47] T. Skála, F. Šutara, M. Škoda, K. C. Prince, and V. Matolín, J. Phys.: Condens. Matter **21**, 055005 (2009).

[48] E. J. Preisler, O. J. Marsh, R. A. Beach, and T. C. McGill, J. Vac. Sci. Technol., B **19**, 1611 (2001).

[49] Z. Wu, M. Li, and S. H. Overbury, J. Catal. **285**, 61 (2012).

[50] J. Li, Z. Zhang, W. Gao, S. Zhang, Y. Ma, and Y. Qu, ACS Appl. Mater. Interfaces **8**, 22988 (2016).

[51] J. H. Yoo, S. W. Nam, S. K. Kang, Y. H. Jeong, D. H. Ko, J. H. Ku, and H. J. Lee, Microelectron. Eng. **56**, 187 (2001).

[52] I. Iordanova, L. Popova, P. Aleksandrova, G. Beshkov, E. Vlahkov, R. Mirchev, and B. Blagoev, Thin Solid Films **515**, 8078 (2007).

[53] L. Luo, J. Chen, and X. Wang, Appl. Surf. Sci. **322**, 111 (2014).

[54] M. Vorokhta, I. Matolínová, M. Dubau, S. Haviar, I. Khalakhan, K. Ševčíková, T. Mori, H. Yoshikawa, and V. Matolín, Appl. Surf. Sci. **303**, 46 (2014).

[55] C. Anandan and P. Bera, Appl. Surf. Sci. **283**, 297 (2013).

[56] P. Bera and C. Anandan, RSC Adv. **4**, 62935 (2014).